The Astrophysical Journal, 879:13 (16pp), 2019 July 1 https://doi.org/10.3847/1538-4357/ab22c1

Using Surface Brightness Fluctuations to Study Nearby Satellite Galaxy Systems: Calibration and Methodology

Scott G. Carlsten[1], Rachael L. Beaton[1,2,4], Johnny P. Greco[3,5], and Jenny E. Greene[1]
[1] Department of Astrophysical Sciences, 4 Ivy Lane, Princeton University, Princeton, NJ 08544, USA; scottgc@princeton.edu
[2] The Observatories of the Carnegie Institution for Science, 813 Santa Barbara St., Pasadena, CA 91101, USA
[3] Center for Cosmology and AstroParticle Physics (CCAPP), The Ohio State University, Columbus, OH 43210, USA
Received 2019 January 19; revised 2019 April 18; accepted 2019 April 22; published 2019 June 28

Abstract

We explore the use of ground-based surface brightness fluctuation (SBF) measurements to constrain distances to nearby dwarf galaxies. Using archival CFHT Megacam imaging data for a sample of 28 nearby dwarfs, we demonstrate that reliable SBF measurements and distances accurate to 15% are possible even for very low surface brightness ($\mu_{0i} > 24$ mag arcsec^{-2}) galaxies with modest, ∼hour-long exposures with CFHT. Combining our sample with a recent sample of six dwarfs with SBF measured with *Hubble Space Telescope* (*HST*) from the literature, we provide the most robust empirical SBF calibration to date for the blue colors expected for these low-mass systems. Our calibration is credible over the color range $0.3 \lesssim g - i \lesssim 0.8$ mag. It is also the first SBF calibration tied completely to tip of the red giant branch (TRGB) distances as each galaxy in the sample has a literature TRGB distance. We find that even though the intrinsic scatter in SBF increases for blue galaxies, the rms scatter in the calibration is still $\lesssim$0.3 mag. We verify our measurements by comparing with *HST* SBF measurements and detailed image simulations. We argue that ground-based SBF is a very useful tool for characterizing dwarf satellite systems and field dwarfs in the nearby, $D \lesssim 20$ Mpc universe.

Key words: galaxies: distances and redshifts – galaxies: dwarf – methods: observational – techniques: photometric

1. Introduction

The dwarf satellite system of the Milky Way (MW) has long been used to test ΛCDM predictions for small-scale structure formation. From the many tensions between theory and observations that have arisen over the past two decades (see Bullock & Boylan-Kolchin 2017, for a recent review), it is clear that gaining a full understanding of galaxy formation at the low-mass end will require a statistical sample of well-characterized satellite systems around galaxies both similar and dissimilar to the MW. While the well-known missing satellites problem and the too big to fail problem appear to be solved for the MW by the addition of baryonic physics (e.g., Macciò et al. 2010; Wetzel et al. 2016), it is possible that the baryonic prescriptions are overtuned to reproduce the specific properties of Local Group (LG) dwarfs. Additionally, the planes of satellites problem (Pawlowski 2018) has recently been highlighted as a small-scale problem that is not solved by the inclusion of baryonic physics in cosmological simulations. It is currently unclear how the presence of a thin, corotating plane of satellite galaxies around the MW (Pawlowski et al. 2012), M31 (Ibata et al. 2013), and Centaurus A (Müller et al. 2018b) fits into the ΛCDM paradigm. Further understanding in all of these problems requires a larger sample of dwarf satellites in a wider variety of systems.

Progress in characterizing dwarf galaxy populations outside of the LG has been made by several groups (e.g., Crnojević et al. 2014; Carlin et al. 2016; Bennet et al. 2017; Danieli et al. 2017; Geha et al. 2017). From this work, it is clear that the two main roadblocks are (1) finding very low surface brightness (LSB) objects within the virial radius of nearby galaxies (which can project to several degrees on the sky) and (2) confirming that the discovered objects are actually physically associated with a given host and not background contaminants. Recent follow-up studies have highlighted the importance of this second issue. Merritt et al. (2016) found with *Hubble Space Telescope* (*HST*) follow-up that four out of seven LSB galaxies discovered with the Dragonfly telescope array (Abraham & van Dokkum 2014) around M101 ($D = 7$ Mpc) were, in fact, background galaxies likely associated with the more distant NGC 5485 group. Similarly, *HST* follow-up by Cohen et al. (2018) found that four out of five LSB galaxies around NGC 4258 were in the background. Clearly, characterizing the number and properties of dwarfs outside the LG requires an accurate grasp of the distance to these LSB objects.

Currently used methods to verify group membership include (1) extensive spectroscopic follow-up to all candidate galaxies (e.g., Spencer et al. 2014; Geha et al. 2017), (2) selecting satellites on size and surface brightness cuts that mimic the LG dwarf population (e.g., Bennet et al. 2017; Müller et al. 2017a, 2017b, 2018a; Kondapally et al. 2018; Tanaka et al. 2018), (3) *HST* follow-up for tip of the red giant branch (TRGB) or surface brightness fluctuation (SBF) distances (e.g., Danieli et al. 2017; Cohen et al. 2018; van Dokkum et al. 2018b), (4) deep ground-based TRGB distances for nearby systems (e.g., Crnojević et al. 2014; Sand et al. 2014; Carlin et al. 2016; Smercina et al. 2017, 2018; Martinez-Delgado et al. 2018; Müller et al. 2018c), and (5) statistical subtraction of a background LSB galaxy density (e.g., Speller & Taylor 2014; Park et al. 2017; Tanaka et al. 2018; Xi et al. 2018). Each of these methods has significant drawbacks. Method 1 requires expensive telescope time and is difficult for quenched, very LSB dwarfs. Method 2 can only determine the distance to roughly a factor of two and will bias any comparison of the dwarf population of other groups to that of the LG. Method 3 requires expensive telescope time since generally only one candidate can be imaged at a time owing to *HST*'s small field of

[4] Hubble Fellow.
[5] NSF Astronomy & Astrophysics Postdoctoral Fellow.

view. Method 4 is limited to nearby ($D \lesssim 4$ Mpc) systems where the virial volume takes up a large solid angle in the sky and, therefore, is difficult to completely survey. Finally, method 5 is a successful strategy for statistical results like luminosity functions (LFs) but is not suitable for measurements requiring specific properties of member systems, such as determining properties of a particular satellite system.

An alternative, promising possibility to efficiently determine distances to LSB dwarfs is ground-based SBF measurements. SBF essentially entails measuring how bumpy or smooth a galaxy's light profile is due to the galaxy being made of discrete stars. Since the fluctuations in the profile come from Poisson statistics in the number of stars in each resolution element, this measurement depends on the distance to the galaxy and the dominant stellar population. The dependence of SBF on the age and metallicity of the galaxy's dominant stellar population is generally accounted for in a color-dependent calibration formula. SBF is appealing because distances can be measured from the same images in which the LSB galaxies are discovered and ground-based SBF is possible to at least twice the distance of ground-based TRGB, since fully resolved stars are not needed. Ground-based SBF has had a long history (e.g., Tonry & Schneider 1988; Tonry et al. 2001; Cantiello et al. 2018) and was pointed out early to have potential for determining the distance to dwarf spheroidal galaxies in the Local Volume. Work by multiple groups (e.g., Jerjen et al. 1998, 2000, 2001, 2004; Jerjen 2003; Mieske et al. 2003, 2006, 2007; Rekola et al. 2005; Dunn & Jerjen 2006) derived calibrations, measured the distance to Local Volume field dwarfs, and used SBF to determine group membership of dEs. Their calibrations either were based on theoretical stellar population synthesis (SPS) models or assumed group membership of dwarfs in Fornax or Virgo. These calibrations were very uncertain and, in the case of the theoretical calibration of Jerjen et al. (2001), did not agree with later SPS models. Since these early works, ground-based SBF has not been used to determine distances and group membership for LSB dwarfs. Instead, the emphasis has been on measuring SBF with *HST*. The time has come to revisit ground-based SBF given that in several cases the data used to discover the LSB dwarfs are of appropriate depth and quality for SBF measurements (e.g., Kim et al. 2011; Bennet et al. 2017; Greco et al. 2018b), as we demonstrate in this paper.

There are two main obstructions to using SBF in this way: (1) the LSB nature of the dwarfs makes the SBF signal noisy since the signal is normalized by the (very low) galaxy mean surface brightness and careful measurements that consider all sources of contamination to the SBF signal are required and (2) most LSB dwarf satellites are significantly bluer than the cluster ellipticals on which most existing SBF calibrations are based. The uncertainty and spread in the calibrations increase significantly in the blue (Mei et al. 2005a; Mieske et al. 2006; Blakeslee et al. 2009, 2010; Jensen et al. 2015; Cantiello et al. 2018). The uncertainty in extrapolating existing calibrations toward bluer colors has recently been highlighted in the contention over the distance to NGC 1052-DF2 (Blakeslee & Cantiello 2018; van Dokkum et al. 2018a; Trujillo et al. 2019) and the conclusion that the galaxy has an anomalously low mass-to-light ratio.

In this paper, we address these limitations by measuring the SBF signal for a wide variety of nearby LSB dwarfs ($D < 12$ Mpc) that have archival CFHT MegaCam/MegaPrime imaging (Boulade et al. 2003). These galaxies were chosen to have TRGB distances, so we provide an absolute SBF calibration based on the TRGB suitable for the low-mass dwarf galaxies. Jerjen et al. (2001) used a few TRGB distances to derive an offset for their otherwise theoretical SBF calibration, and Cantiello et al. (2007a) used a handful of TRGB distances to determine which (at that time) existing absolute calibration performed the best, but the calibration we derive is the first based solely on TRGB distances. Previous SBF calibrations are based on Cepheid distances that derive from younger stellar populations than the SBF signals do and therefore involve additional systematic uncertainties in the calibration.

This paper is structured as follows: in Section 2 we describe our data selection and sample, in Section 3 we describe our SBF measurement methodology, in Section 4 we present our SBF calibration and compare with stellar population models, and in Section 5 we discuss the results in the context of determining the distance to LSB galaxies and conclude.

2. Data

We start the galaxy selection with the Nearby Galaxy Catalog of Karachentsev et al. (2013). We restrict our sample to galaxies that have measured TRGB distances in the range 2.5 Mpc $< D <$ 12 Mpc. The lower bound is to eliminate galaxies that are so resolved that the SBF would be very difficult to measure, as a smooth background brightness profile of a galaxy could not be estimated.[6] We supplement this catalog with the recent sample of satellites around NGC 4258 and M96 from Cohen et al. (2018) and Do1 from Martinez-Delgado et al. (2018).

Each galaxy is searched for in the CFHT MegaCam archive,[7] and only galaxies with both *g*- and *i*-band archival imaging are used. *i* band is a common choice for measuring SBF, as it is a middle ground between the competing factors that SBF is brighter and seeing is generally better for redder passbands (e.g., Jensen et al. 2003; Carlsten et al. 2018), whereas the instrumental efficiency and the sky foreground become limiting factors in the infrared. Additionally, previous work has shown that degeneracy between stellar population age and metallicity makes the scatter in the SBF calibration smallest in the *i* band (Jensen et al. 2003, 2015) and the SBF magnitude–color slope is minimized in the near-IR (Cantiello et al. 2003). We therefore measure SBF in the *i* band and use the $g-i$ color to parameterize the SBF's dependence on the stellar population. MegaCam has had several generations of *g* and *i* filters since first light in 2003. We accept galaxies imaged in any of the three *i* filters used (I.MP9701, I.MP9702, and I.MP9703) and either of the two *g* filters (G.MP9401 and G.MP9402). For galaxies that have imaging in more than one *g* or *i* filter, we choose the filter with the most exposure time so that each galaxy uses imaging done in only one filter. We show in Appendix C that the difference between the filters has an impact smaller than 0.07 mag, and, in consequence, we do not attempt to correct for this or try to convert all the *i*- or *g*-band data to a specific *i* or *g* filter. All of the different *i* and *g* filters are treated equally in the subsequent analysis. This 0.07 mag offset between filters is comparable to the intrinsic scatter in SBF (Blakeslee et al. 2009) but, as shown

[6] Note that for resolved galaxies, it is possible to measure the SBF as a discrete sum of individual stars (e.g., Ajhar & Tonry 1994) without the need for a smooth galaxy profile. However, since the calibration we derive will be used for more distant galaxies, we only consider measuring the SBF in a way that is possible for unresolved galaxies, which requires a model for the smooth galaxy profile.

[7] http://www.cadc-ccda.hia-iha.nrc-cnrc.gc.ca/en/

Table 1
Main Galaxy Sample

Name	R.A.	Decl.	Distance (Mpc)	μ_{0i} (mag arcsec^{-2})	r_e (arcsec)	$g-i$	M_i (mag)	$t_{\rm exp}$ (s)	Multinight i/g
FM1	09:45:10.0	+68:45:54	3.78	24.4 ± 0.1	24.1	0.51 ± 0.1	−11.8 ± 0.1	660.6	y/n
UGC 004483	08:37:03.0	+69:46:31	3.58	22.3 ± 0.1	27.6	−0.02 ± 0.1	−13.3 ± 0.1	600.5	n/y
KDG 061	09:57:02.7	+68:35:30	3.66	23.9 ± 0.1	35.3	0.39 ± 0.1	−12.6 ± 0.1	20003.1	y/y
BK5N	10:04:40.3	+68:15:20	3.7	24.3 ± 0.1	24.4	0.52 ± 0.1	−11.6 ± 0.1	1101.1	n/y
LVJ1228+4358	12:28:44.9	+43:58:18	4.07	25.0 ± 0.1	50.1	0.55 ± 0.1	−12.1 ± 0.1	1800.8	n/y
DDO 125†	12:27:41.9	+43:29:58	2.61	22.5 ± 0.1	68.7	0.1 ± 0.1	−14.5 ± 0.1	1800.8	n/y
UGCA 365	13:36:30.8	−29:14:11	5.42	22.1 ± 0.1	27.5	0.47 ± 0.1	−14.2 ± 0.1	161.1	n/n
M94_dw2	12:51:04.4	+41:38:10	4.7	24.6 ± 0.1	10.9	0.61 ± 0.1	−9.8 ± 0.1	644.7	n/n
DDO 044	07:34:11.3	+66:53:10	3.21	24.2 ± 0.1	46.9	0.69 ± 0.1	−12.6 ± 0.1	1000.9	n/n
NGC 4163†	12:12:08.9	+36:10:10	2.99	20.9 ± 0.1	30.2	0.58 ± 0.1	−14.6 ± 0.1	3601.5	n/n
NGC 4190†	12:13:44.6	+36:37:60	2.83	20.5 ± 0.1	26.2	0.52 ± 0.1	−14.7 ± 0.1	3601.5	n/n
KDG 090	12:14:57.9	+36:13:08	2.98	23.7 ± 0.1	38.3	0.8 ± 0.1	−12.6 ± 0.1	3601.5	n/n
UGC 08508†	13:30:44.4	+54:54:36	2.67	21.8 ± 0.1	30.5	0.37 ± 0.1	−13.6 ± 0.1	2701.3	y/n
DDO 190†	14:24:43.5	+44:31:33	2.83	22.1 ± 0.1	32.3	0.52 ± 0.1	−14.4 ± 0.1	4001.7	n/n
KKH 98	23:45:34.0	+38:43:04	2.58	23.2 ± 0.1	21.8	0.08 ± 0.1	−11.7 ± 0.1	6752.7	y/y
Do1	01:11:40.4	+34:36:03	3.3	25.6 ± 0.1	14.3	0.33 ± 0.1	−9.1 ± 0.1	3211.6	y/y
LVJ1218+4655†	12:18:11.1	+46:55:01	8.28	22.1 ± 0.1	19.0	0.31 ± 0.1	−13.3 ± 0.1	8294.0	y/y
NGC 4258_DF6	12:19:06.5	+47:43:51	7.3	24.4 ± 0.1	8.7	0.62 ± 0.1	−11.0 ± 0.1	8294.0	y/y
KDG 101	12:19:09.1	+47:05:23	7.28	22.7 ± 0.1	26.6	0.68 ± 0.1	−14.8 ± 0.1	8294.0	y/y
M101_DF1	14:03:45.0	+53:56:40	6.37	24.5 ± 0.1	15.1	0.71 ± 0.1	−11.0 ± 0.1	4571.6	y/y
M101_DF2	14:08:37.5	+54:19:31	6.87	25.0 ± 0.1	9.3	0.69 ± 0.1	−10.5 ± 0.1	8612.7	y/y
M101_DF3	14:03:05.7	+53:36:56	6.52	25.7 ± 0.1	30.9	0.47 ± 0.1	−11.8 ± 0.1	4306.3	n/y
UGC 9405†	14:35:24.1	+57:15:21	6.3	23.1 ± 0.1	46.9	0.56 ± 0.1	−15.1 ± 0.1	4306.4	n/n
M96_DF9	10:46:14.2	+12:57:38	10.0	24.0 ± 0.1	8.3	0.79 ± 0.1	−12.1 ± 0.1	714.6	y/y
M96_DF1	10:48:13.1	+11:58:06	10.4	24.2 ± 0.1	8.6	0.57 ± 0.1	−11.3 ± 0.1	3930.6	y/y
M96_DF8	10:46:57.4	+12:59:55	10.2	23.9 ± 0.1	27.8	0.67 ± 0.1	−14.4 ± 0.1	2510.7	y/y
M96_DF4	10:50:27.2	+12:21:35	10.0	24.3 ± 0.1	22.3	0.61 ± 0.1	−13.8 ± 0.1	952.7	y/y
M96_DF5	10:49:26.0	+12:33:10	10.8	23.6 ± 0.1	28.2	0.83 ± 0.1	−13.1 ± 0.1	3344.3	y/y
M96_DF7	10:47:13.5	+12:48:09	10.2	25.5 ± 0.1	10.6	0.57 ± 0.1	−11.2 ± 0.1	2929.9	y/y
M96_DF10	10:48:36.0	+13:03:35	10.6	25.2 ± 0.1	12.3	0.77 ± 0.1	−11.7 ± 0.1	1915.2	y/y
M96_DF6	10:46:53.1	+12:44:34	10.2	25.5 ± 0.1	23.1	0.37 ± 0.1	−12.7 ± 0.1	4001.8	y/y
M96_DF2	10:47:40.6	+12:02:56	10.6	25.0 ± 0.1	6.6	1.12 ± 0.1	−10.7 ± 0.1	4645.3	y/y

Note. For galaxies indicated with a †, the Sérsic profiles were explicitly fit in the outer regions, the reported surface brightness might not be representative of the actual center, and the total magnitude (which comes from the Sérsic fit) might underestimate the actual galaxy. The "Multinight" column indicates whether the data were taken contiguously in one night or over multiple nights. More information on the CFHT data used for each galaxy, including P.I., proposal I.D., and specific filters, is given in Table 2 in Appendix B. The distances come from Karachentsev et al. (2013), except for the M96 dwarfs and NGC 4258_DF6, which come from Cohen et al. (2018), and Do1, which comes from Martinez-Delgado et al. (2018). The photometry comes from our own measurements.

below, is significantly smaller than the other uncertainties involved in the measurements and therefore is unimportant in the current study. However, we note that this level of precision will be important in future studies that are able to measure SBF with higher precision, perhaps from space. All photometry is given in the AB system. Unless stated otherwise, all photometry is corrected for Galactic extinction using the $E(B-V)$ values from Schlegel et al. (1998) recalibrated by Schlafly & Finkbeiner (2011).

The galaxies are visually inspected, and ones with significant substructure[8] that would make SBF measurements difficult are removed. We list the rejected galaxies along with the reason for rejection in Appendix D. We are left with a sample of 32 galaxies, which are listed in Table 1. The sample is inhomogeneous, spanning a range of color, surface brightness, and exposure time.

The default MegaCam pipeline, `MegaPipe` (Gwyn 2008), is unsuitable for SBF measurements, as it performs a very aggressive, local background subtraction that mistakes large LSB galaxies for sky foreground and subtracts them out (e.g., Ferrarese et al. 2012). We therefore start with the `Elixir` (Magnier & Cuillandre 2004) pre-processed CCD frames and perform the sky subtraction and stacking ourselves. The `Elixir` pre-processed images have had the instrumental signatures removed and have been flat-fielded. The images are also given a rough astrometric and photometric calibration. We improve on the astrometric solution by matching sources with SDSS-DR9 (Ahn et al. 2012) sources or USNO-B1 (Monet et al. 2003) for galaxies outside of the SDSS footprint, using the `Scamp` (Bertin 2006) software. The astrometric solutions generally have residuals less than 0.″15 rms. The photometric zero-point for each CCD frame is set by matching sources with SDSS-DR14 (Abolfathi et al. 2018) or Pan-STARRS1-DR1 (Chambers et al. 2016) for sources outside of the SDSS footprint. SDSS and Pan-STARRS1 magnitudes are converted to the MegaCam photometric system using transformation equations[9] that come from a variety of synthetic and empirical

[8] Including dust lanes, spiral structure, and clumpy star-forming regions.

[9] Available online at http://www.cadc-ccda.hia-iha.nrc-cnrc.gc.ca/en/megapipe/docs/filt.html.

spectral libraries of stars and galaxies. The residuals for the photometry are generally less than 0.05 mag.

The sky subtraction procedure is based on that of the `Elixir-LSB` pipeline (e.g., Ferrarese et al. 2012; Duc et al. 2015). The observed background comes from reflections of the sky background in the optics and the flat-fielding process, leading to a radial, "eye"-like pattern on the focal plane. It changes as the sky level changes but is constant over timescales of a couple hours. We utilize this constancy in time to determine a sky frame for each CCD that is near or covers the galaxy being processed. The data have widely varied dithering patterns, but generally there are more than five exposures in each filter dithered by 10″–20″. These dither sizes are significantly smaller than those used in Ferrarese et al. (2012) or Duc et al. (2015), so large objects ($\gtrsim$10″) would persist after taking the median of the dithered exposures. Therefore, we mask sources with `SExtractor` (Bertin & Arnouts 1996). This helped prevent large sources from "leaking" into the model of the sky foreground. We then median-combine these exposures for each CCD after scaling by the mode to generate the sky frame for that CCD. This sky frame can then be rescaled for each individual exposure and subtracted out. The background-subtracted images are resampled and median-combined with a `Lanczos3` interpolation kernel using `SWarp` (Bertin 2010). Roughly one-third of the galaxies have data that were taken consecutively over a few hours, which is the scenario for which the above procedure was designed. The remaining roughly 2/3 of the galaxies have data taken from multiple research groups spanning many nights, possibly over several years. The background pattern changes on these timescales; however, we find with the simulations described in Appendix A that the measurements of the galaxy color and SBF magnitude are not significantly affected by background subtraction errors.

Once the data are astrometrically and photometrically calibrated and co-added, cutouts around the galaxies are made, which are then ready for the SBF measurement.

3. SBF Measurement

In brief, measuring the SBF entails quantifying the brightness fluctuations relative to the smooth galaxy profile. Fluctuations are due to the Poisson statistics in the number of RGB and AGB stars in each resolution element. In line with the common definition, we determine the absolute SBF magnitude for each system, which is defined for a stellar population as

$$\bar{M} = -2.5\log\left(\frac{\sum_i n_i L_i^2}{\sum_i n_i L_i}\right) + \text{z.p.}, \quad (1)$$

where n_i is the number of stars with luminosity L_i in the stellar population and z.p. is the zero-point of the photometry. The absolute SBF magnitude depends on the age and metallicity of the dominant stellar population of a galaxy. The goal of the current project is to relate the absolute SBF magnitude to the color of the stellar population, which will account for its dependence on age and metallicity.

In this section, we describe the major steps in quantifying the SBF. Many of these are standard techniques, though some are particular to our application of SBF to very LSB galaxies.

3.1. Sérsic Fits and Masking

Since a model for the smooth profile of the galaxy is required, the first step in measuring the SBF is fitting a Sérsic profile to each galaxy. We find that a nonparametric fit to the smooth profile using, for example, elliptical isophotes (Jedrzejewski 1987) was not possible for many of the faint dwarf galaxies analyzed here and similarly will not be possible for many faint satellite galaxies that are a primary motivation for the current work. Many of the galaxies in the sample were too faint and small for elliptical isophotes to be robustly fit. For consistency, we therefore use single Sérsic profiles as models for the smooth galaxy background profile for all galaxies in our sample. Cohen et al. (2018) use this approach as well. As described above, galaxies that display strongly nonaxisymmetric profiles or otherwise visibly deviate from a Sérsic profile are not included in the analysis. As discussed more below, many galaxies will still have subtle deviations from Sérsic profiles, and this contributed to the scatter of the calibration. For some of the included galaxies, the central regions had complicated clumpy structure, whereas the outer regions were well described by a smooth Sérsic. For these galaxies, the central surface brightness given in Table 1 comes from fitting the outer regions while masking the inner regions and might not be representative of the actual central surface brightness. `Imfit` (Erwin 2015) is used to do the fitting. Because it is generally deeper, the *g*-band image is always fit first, and then only the normalization of the Sérsic profile is allowed to vary when fitting the *i*-band image.

Once a Sérsic profile is fit to each galaxy, it is subtracted and point sources in the image are detected and masked using `sep`[10] (Barbary 2016), a Python implementation for SExtractor (Bertin & Arnouts 1996). The masking removed contributions to the brightness fluctuations from foreground stars, star clusters in the galaxy analyzed, and background galaxies. Choosing the masking threshold requires some care, as too high of a threshold will leave many sources that bias the fluctuation measurement to larger values, erroneously reducing the measured distance, and too low of a mask might actually mask some of the brightest SBF. Instead of choosing a fixed threshold defined in terms of standard deviations above the background, we set the mask at a certain absolute magnitude level at the distance of the galaxy. Globular clusters (GCs) will have $M_i \sim -8$ mag, while the brightest RGB stars will have $M_i \sim -4$ mag. Therefore, there is much room between those magnitudes to set a masking threshold that masks GCs while not masking SBF.

We note that the GC luminosity function (GCLF) is Gaussian and GCs fainter than $M_i \sim -8$ mag exist. However, the low-mass galaxies that constitute our sample are expected to have few, if any, GCs (Forbes et al. 2018). A mask threshold 1 or 2 mag below the peak of the GCLF will therefore mask essentially every GC present. As a quantitative demonstration of this, the brightest galaxy in our sample has $M_i \sim -15$, which will have $M_V \sim -15$. This is approximately the magnitude of the Sagittarius dSph of the MW. The Sgr dSph has eight known GCs (Law & Majewski 2010; Forbes et al. 2018), which is then an upper limit to the number of GCs expected for any galaxy in our sample. If we assume a Gaussian GCLF with peak at $M_i \sim -8$ and standard deviation of 1 mag, an absolute magnitude threshold of $M_i \sim -6$ will

[10] https://github.com/kbarbary/sep

mask ∼98% of GCs, which, if there are $\lesssim$8, will essentially be all of them.

Foreground stars and background galaxies are less of a concern since the fluctuation signal in a background control field is subtracted out, as described below. For all the galaxies we mask the images down to sources that would have absolute magnitudes in the range of −4 to −6. The specific threshold in that range is chosen on a per-galaxy basis to ensure that bright objects that visually do not look like SBF within the galaxy are masked. For cases where it was ambiguous whether some sources should be masked or not, multiple thresholds were used. These different thresholds were combined and incorporated into the measurement uncertainty in the Monte Carlo procedure described in Section 3.3. These threshold magnitudes correspond to thresholds of 2–10 standard deviations above the sky background, depending on the depth of the data for a particular galaxy. The same magnitude threshold is used for each of the *g* and *i* bands, and the detection masks are merged between both the filters. As described below in Section 3.5, we use image simulations to demonstrate that this masking procedure does not cause any significant bias to the SBF measurement.

3.2. Fluctuation Measurement

After the galaxy has a Sérsic fit and is masked, we normalize the image by dividing by the square root of the galaxy model. Then, we measure the SBF variance in the usual way by Fourier transforming the image and calculating the 1D azimuthally averaged power spectrum. This power spectrum is fit by a combination of the power spectrum of the point-spread function (PSF) model convolved with the power spectrum of the mask and a constant, representing the power spectrum of (white) photometric noise. Due to the pixel interpolation in the stacking procedure, the photometric noise is not actually white, but using a `Lanczos3` interpolation kernel minimizes the correlations in the noise (Cantiello et al. 2005; Mei et al. 2005b). We model the PSF at the location of each galaxy using the image of a nearby, unsaturated star. We have checked that the choice of star does not significantly affect the measured SBF signal by simply choosing different high signal-to-noise ratio (S/N), nearby, unsaturated stars. We did this experiment for five different galaxies with different surface brightness, colors, and sizes and found that the measured SBF magnitudes using different PSF stars had rms differences <0.1 mag in all cases and often <0.05 mag. While it would be possible to include this in the measurement uncertainties, this effect is similar in magnitude to the uncertainty due to different CFHT *i* filters ($\lesssim$0.07 mag), and we opt to not include it. The area of the galaxy used in the fit depends on the galaxy. For most of the LSB galaxies with $\mu_{i0} > 23$ mag arcsec^{-2}, the galaxy is fit out to the radius where it falls below 0.4 times the central brightness of the galaxy. This was found to roughly maximize the S/N of the SBF measurement for these faint galaxies. For the galaxies with non-Sérsic centers, an annulus was used that avoided the central region. The fitted regions had radii anywhere between 50 and 250 pixels (10″–50″), depending on the size of the galaxy.

Unlike the usual approach (e.g., Tonry et al. 2001; Blakeslee et al. 2009; Cantiello et al. 2018), we do not attempt to model the contribution to the fluctuation signal from undetected (and, hence, unmasked) GCs and background galaxies. Instead, we measure the fluctuation signal in nearby fields and subtract this residual level from the signal measured from the galaxy. This approach will remove the residual signal due to unmasked background galaxies and foreground MW stars but will not correct for GCs associated with the galaxy. Since our galaxies are primarily very low mass dwarfs, they are not expected to have many GCs (Forbes et al. 2018). The existing ones are bright enough to be easily detected and masked, and so GCs and other star clusters are not a concern for these galaxies. This background field approach has the benefit of also accounting for the residual variance due to the correlated noise in the resampling process.

3.3. Uncertainty in SBF Measurement

The uncertainty in the SBF measurement comes from two main sources: (1) the uncertainty in the actual power spectrum fit for the galaxy and (2) the stochasticity in the residual signal from unmasked sources. In this section, we describe how we include both sources in our final SBF measurement uncertainty.

Following Cohen et al. (2018), we estimate the error in fitting for the SBF magnitude of the galaxy by slightly altering at random the area of the galaxy used and the range of wavenumbers fit in the power spectrum in a Monte Carlo approach. Each galaxy's power spectrum was fit 100 times, with each iteration using a slightly different annulus (centered on the fiducial area chosen for each galaxy, as described above) and different lower and upper wavenumbers. The lower wavenumber was chosen in the range of 0.03–0.08 pixels^{-1}, and the upper wavenumber was chosen in the range of 0.3–0.4 pixels^{-1}. The measurements in different annuli are not independent. However, this is fine, as we are using the spread in the different annuli to quantify the uncertainty in the measurement. For the galaxies in which we used multiple masking thresholds, one of the masking thresholds is chosen at random for each Monte Carlo trial. In this way, the uncertainty in the mask is reflected in the uncertainty in the SBF measurement.

We are in a different regime than most SBF studies (e.g., Tonry et al. 2001; Blakeslee et al. 2009; Cantiello et al. 2018) because our galaxies are much smaller than the big ellipticals usually studied. Therefore, the randomness in the residual signal from unmasked sources contributes significantly to the error in the SBF measurement. To include this in our estimate of the uncertainty of the SBF signal, we measure the SBF in a grid of nearby background fields. The background fields are masked and normalized just like the galaxy (and have the same exposure time and depth). In each of the Monte Carlo trials, one of these fields is randomly chosen and its SBF signal is fit using the annulus and range of wavenumbers used for the galaxy. The measured variance is subtracted from the SBF signal measured from the galaxy.

We take the median of the resulting distribution of corrected SBF variances to be the measured SBF signal and its standard deviation as the uncertainty. The main steps of this procedure are shown in Figure 1 for an example galaxy.

We define a rough estimate of the S/N of the SBF detection simply as the signal divided by the uncertainty. This definition is a little different than previous estimates of the S/N (e.g., Jensen et al. 1998) that involve the amplitude of the constant noise floor, but we use it to emphasize the effect of the stochasticity of the residual variance. Some of the LSB satellites from the Cohen et al. (2018) sample in the M96 system were too faint to detect SBF in the CFHT data. We only used the CFHT SBF measurements for sources with S/N > 2. Five of the M96 group galaxies had measurable SBF above this threshold. The *HST* SBF measurements from Cohen et al. (2018) are used for the other galaxies in the M96 group, as described below in Section 4, where we present the calibration.

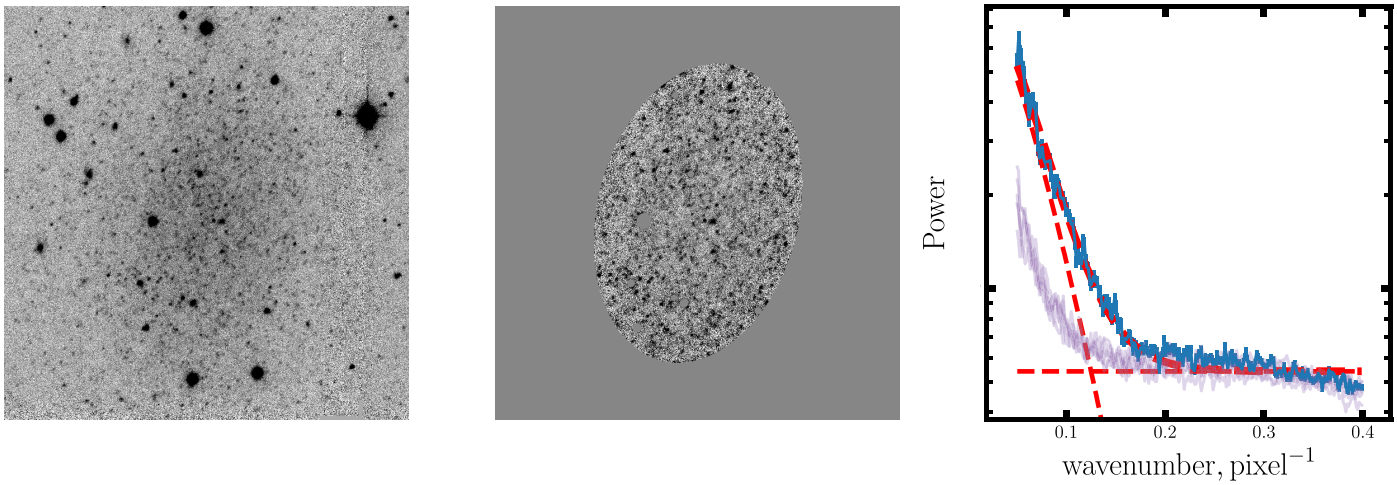

Figure 1. Example of the SBF measurement process for the galaxy DDO 044. The left panel shows the *i*-band image of the galaxy. The middle panel shows the galaxy once the smooth background has been subtracted out, the image divided by the square root of the smooth profile, and the image masked for contaminating sources. The right panel shows the azimuthally averaged power spectrum (in blue) and the best-fitting combination of a white-noise component and PSF component to the variance (dashed red). The power spectrum starts to drop at high wavenumber owing to the correlated noise present in the images. The purple lines show the power spectra measured in the background fields. Note that since we scale all images to have a zero-point of 27, the units of power are arbitrary and therefore not shown.

3.4. *Comparison to* HST *Measurements*

We have six galaxies in our sample for which we could measure the SBF with the CFHT data and that had *HST* SBF measurements from Cohen et al. (2018). These galaxies include one from the NGC 4258 group (NGC 4258_DF6) and five from the M96 group (M96_DF1, M96_DF4, M96_DF5, M96_DF6, M96_DF8). We supplement this sample with two more galaxies from the NGC 4258 area from Cohen et al. (2018) (NGC 4258_DF1 and NGC 4258_DF2) for which CFHT *i*-band data existed. These two are not in the main galaxy sample because they do not have TRGB distances owing to the fact that they are significantly more distant than NGC 4258 (Cohen et al. 2018). As a first verification of our SBF measurements, we compare our measured SBF magnitudes with those measured from the *HST* data for these galaxies in common. We take the measured (apparent) SBF magnitudes in the *HST* I_{814} band from Cohen et al. (2018) and convert to CFHT *i* band via

$$\bar{m}_i^{\rm CFHT} = \bar{m}_{I_{814}}^{HST} + 0.540x^2 - 0.606x + 0.253, \qquad (2)$$

where $x \equiv g_{475} - I_{814}$ is the *HST* galaxy color from Cohen et al. (2018). We derive this formula from simple stellar population (SSP) predictions of the SBF magnitudes in the two filter systems from the MIST isochrones (Choi et al. 2016). The conversion was calculated for SSPs in the age range 3 Gyr < age < 10 Gyr and metallicities in the range $-2 <$ [Fe/H] < 0 and has residuals $\lesssim$0.05 mag. Using the PARSEC isochrones (Bressan et al. 2012) instead would change this conversion by less than 0.04 mag. Note that this conversion is specifically for the I.MP9701 filter. We can then directly compare our measured SBF magnitudes with those from Cohen et al. (2018) converted to the CFHT filter system. Figure 2 shows this comparison for the eight galaxies in common. All galaxies fall on the 1:1 line within their uncertainties and span roughly 2 mag in SBF brightness.

3.5. *Image Simulations*

As an additional check on our SBF measurement process, we performed realistic image simulations to see how well we could recover the color and SBF magnitude of an LSB galaxy. The goal of these simulations is threefold: (1) we explore how well our sky subtraction performs and the accuracy of the measured galaxy colors, (2) we show that the measured SBF magnitude is an unbiased estimator of the true SBF magnitude, and (3) we show that our reported uncertainties are realistic based on the primary sources of error. This last point is a crucial prerequisite to understanding the intrinsic spread in the calibration.

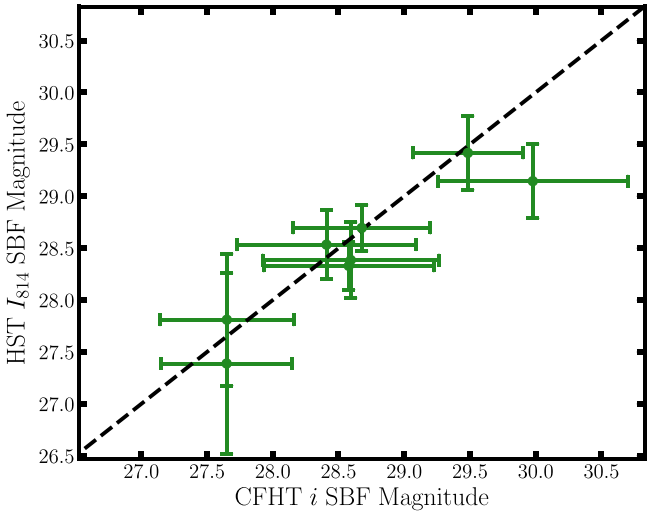

Figure 2. Comparison between the SBF (apparent) magnitudes we measure with the CFHT data and those measured from *HST* data by Cohen et al. (2018) for the eight galaxies in common. The dashed line shows a one-to-one correspondence. Note that since Cohen et al. (2018) do not report measured SBF magnitudes or corresponding uncertainties, the vertical error bars are taken to be the uncertainties in the SBF distance moduli. These are upper bounds to the SBF measurement uncertainties.

We describe the simulation process in detail in Appendix A. We simulated galaxies with the properties of six specific galaxies in our sample: BK5N, NGC 4163, NGC 4258_DF6, M101_DF3, KKH 98, and M94_Dw2. These six were chosen because they have a representative range in surface brightness, size, and exposure time (see Table 1).

As demonstrated in more detail in Appendix A, we find that we recover the colors of the galaxies with an accuracy of

$\sim$0.1 mag, which seems to be the limit set by the sky subtraction process. We use this as a representative uncertainty in the galaxy colors and photometry.

4. SBF Calibration

With the SBF magnitudes measured for each galaxy in the sample, we now turn to the primary motivation of this paper: to derive an empirical SBF calibration that is valid for blue, low-mass dwarf galaxies.

As mentioned above, there were four galaxies in our sample in the M96 system that were too faint to reliably measure SBF from the CFHT imaging. Instead of completely removing these galaxies from the calibration, we use the *HST* SBF measurements from Cohen et al. (2018). In addition to these four, we include two other M96 dwarfs from Cohen et al. (2018) for which there were no CFHT data (M96_DF3 and M96_DF11). We convert the SBF magnitudes from the *HST* I_{814} filter to the CFHT i band with Equation (2). We convert the *HST* color from Cohen et al. (2018) to CFHT $g-i$ with

$$(g-i)^{\rm CFHT} = x - 0.061x^2 - 0.040x - 0.003, \quad (3)$$

where $x \equiv g_{475} - I_{814}$ is the galaxy color from *HST*. Like Equation (2), this expression is derived from SSP models from the MIST project (Choi et al. 2016) in the age range 3 Gyr $<$ age $<$ 10 Gyr and in the metallicity range $-2 <$ [Fe/H] < 0 and has residuals $\lesssim$0.01 mag.

Using the measured TRGB distances, we convert our measured apparent SBF magnitudes to absolute magnitudes. Since the Karachentsev et al. (2013) catalog does not include errors in the TRGB distances, we include a 0.1 mag error in each of the TRGB distances. This is a characteristic random uncertainty in determining the TRGB (see comparisons of TRGB detection methods in Jang et al. 2018 and Beaton et al. 2018 for discussion) but does not account for any systematic uncertainty on the TRGB zero-point. This level of uncertainty agrees well with the TRGB uncertainties quoted by Danieli et al. (2017) and Cohen et al. (2018).

Figure 3 shows the absolute SBF magnitude versus $g-i$ color for all galaxies in our sample. The sample includes 28 galaxies that have SBF measured with CFHT data, supplemented by six galaxies that have SBF measured by *HST*. A clear relation where SBF magnitude is brighter for bluer color is seen. Also shown is the Next Generation Virgo Survey sample of Cantiello et al. (2018) and the range of validity of their calibration. The sample from Cantiello et al. (2018) is restricted to those galaxies with *HST* SBF distances from Blakeslee et al. (2009) and that are in the Virgo Cluster proper (labeled "V" in their Table 2). The apparent $\bar{m}_i$ magnitudes are converted to absolute SBF magnitudes with the distance modulus to Virgo of 31.09 mag used by Blakeslee et al. (2009). We do not use the individual galaxy distances from Blakeslee et al. (2009) because those distances are SBF distances and would mask the intrinsic scatter in the SBF calibration.[11] We explore the intrinsic scatter in more detail in Section 4.1. The fact that almost all of our sample, which is primarily composed of LSB satellites, is bluer than the range of Cantiello et al. (2018) highlights the need for a bluer SBF calibration in order to use SBF to study dwarf satellite systems. The SBF magnitude does not completely flatten out at blue colors but instead appears to get as bright as $\bar{M}_i \sim -3$ mag at the bluest of colors.

The relation between SBF magnitude and color appears to be roughly linear throughout the entire color range (0.3 mag $\lesssim g-i \lesssim$ 1.1 mag). In the presence of significant uncertainties in both SBF magnitude and color, ordinary least-squares minimization is inadequate (e.g., Hogg et al. 2010). Instead, we adopt the Bayesian algorithm `LINMIX` developed by Kelly (2007). In short, the algorithm models the independent variable's density as a Gaussian mixture model that allows one to write a simple likelihood function for the observed data, accounting for general covariance in the independent and dependent variables and intrinsic scatter in the relationship. This allows posterior distributions on the parameters of the linear relationship to be modeled through MCMC sampling. This method does not exhibit the bias that generalized χ^2 minimization methods do (e.g., Tremaine et al. 2002), even when accounting for errors in the independent variable. We use the `python` implementation of `LINMIX` written by J. Meyers.[12] In doing the linear regression, we assume that the measurement errors on color and SBF magnitude are uncorrelated and Gaussian. As shown in Appendix A, the recovered colors and SBF magnitudes in the image simulations are not significantly correlated, so this is likely an accurate assumption. We take uniform priors on the slope, normalization, and intrinsic scatter squared.

In Figure 4 we show the results of the linear regression. Marginalized posterior distributions are shown for the y-intercept and slope. Taking the median of the posteriors and 1σ uncertainties, we find the linear relationship between SBF magnitude and color as

$$\bar{M}_i = (-3.17 \pm 0.19) + (2.15 \pm 0.35) \times (g-i), \quad (4)$$

where the reported error bars are the *marginalized* uncertainties. Note that the slope and zero-point are highly covariant (see bottom left panel of Figure 4). We note that the slope is significantly less than the 3.25 found by Cantiello et al. (2018) for redder galaxies, indicating that the SBF magnitude–color relation does flatten somewhat at bluer colors. The zero-point of Equation (4) does not, as written, include any additional uncertainty from the zero-point of the TRGB distances.

4.1. Scatter of the Calibration

An important consideration in the calibration is the intrinsic scatter. Intrinsic scatter in empirical SBF calibrations has been measured before (e.g., Blakeslee et al. 2009) and is expected theoretically owing to the age and metallicity differences in the stellar populations in the galaxies (see Section 4.2 for further discussion of this point). Numerous previous studies have found that the intrinsic spread increases for blue colors (Mei et al. 2005a; Mieske et al. 2006; Blakeslee et al. 2009, 2010; Jensen et al. 2015; Cantiello et al. 2018). Our TRGB methodology offers the unique capability to measure intrinsic scatter because we are not relying on cluster membership to assign distances to individual galaxies. Empirical calibrations that rely on cluster membership, like those using Virgo Cluster

[11] Note that this argument assumes that the SBF magnitude in CFHT i band correlates strongly with that in *HST* z band (the passband that Blakeslee et al. 2009 uses). In other words, if a galaxy has anomalously bright SBF in the i band, it would have anomalously bright SBF in the z band as well. This is likely the case, as Blakeslee et al. (2010) have shown that *HST I* correlates strongly with *HST* z band.

[12] https://github.com/jmeyers314/linmix

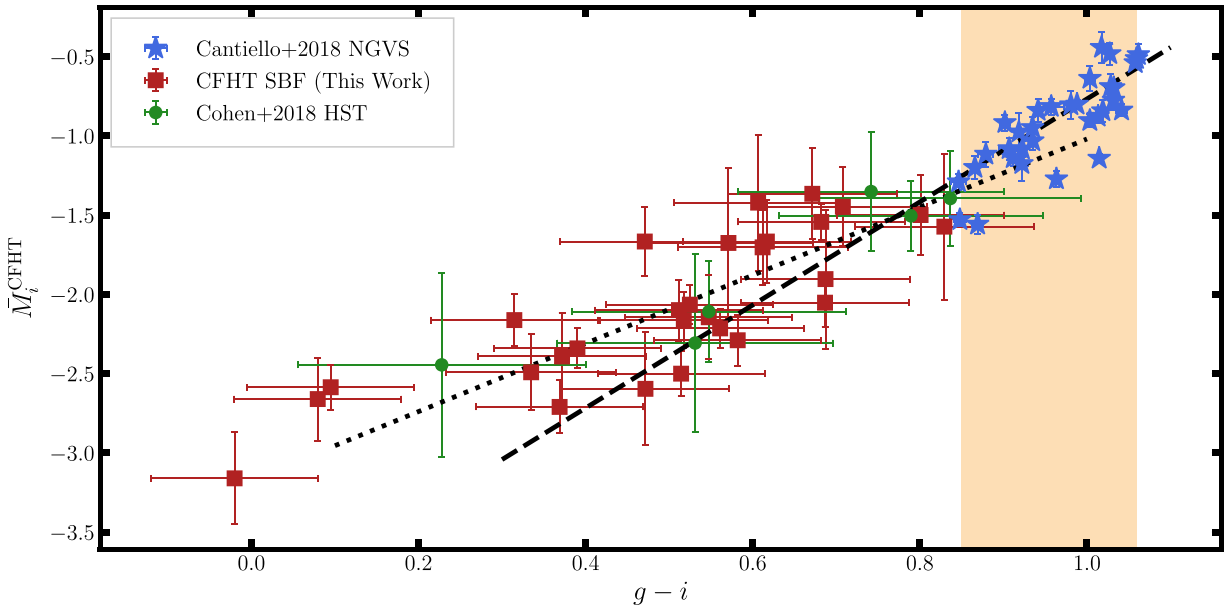

Figure 3. Absolute SBF magnitude vs. $g-i$ color for our entire sample, including six galaxies with SBF measured by Cohen et al. (2018) for which the CFHT imaging was too shallow to measure ground-based SBF. Also shown is the NGVS sample of Cantiello et al. (2018). The orange shaded region is the extent of the calibration from Cantiello et al. (2018), demonstrating the need for bluer calibrations. The dashed black line shows the calibration from Cantiello et al. (2018). The dotted black line shows our best-fitting calibration given in the text.

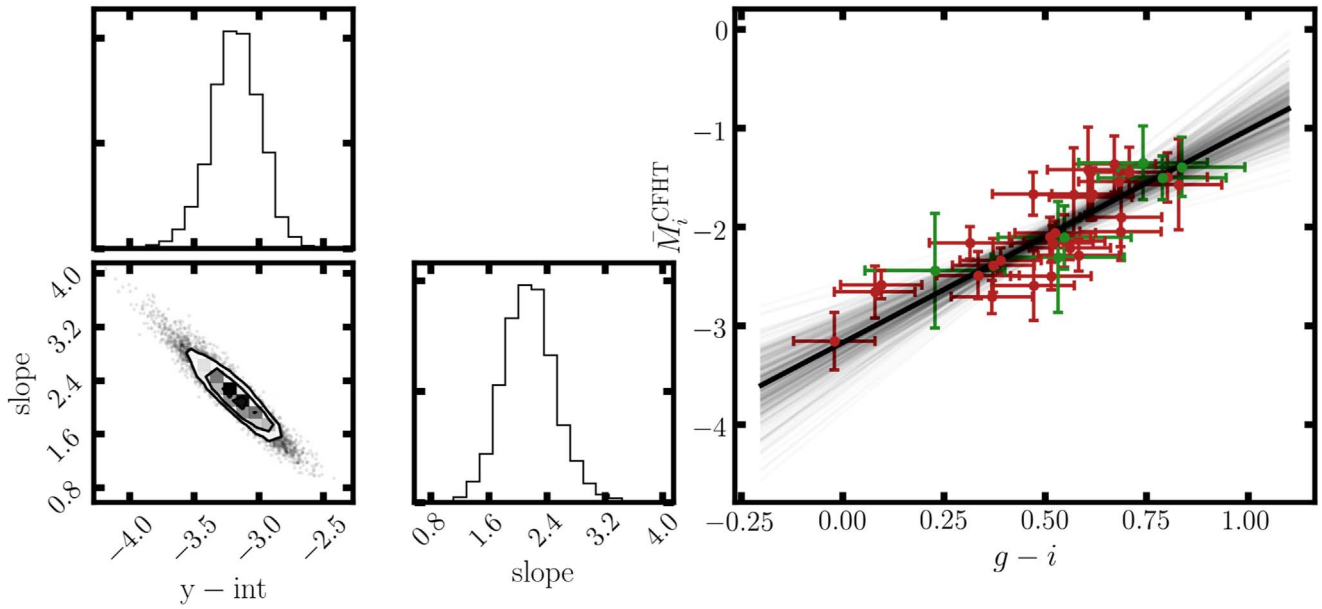

Figure 4. Results of linear regression for the LSB sample. The left side of the plot shows the posterior distributions from the MCMC samples. The right side shows the SBF magnitude–color relationship for the LSB sample (colors are the same as in Figure 3). The thick black line is the median relation from the linear regression, and the thin black lines show random samples from the MCMC chains. `corner` (Foreman-Mackey 2016) was used to visualize the posteriors.

galaxies (e.g., Blakeslee et al. 2009; Cantiello et al. 2018), have to disentangle the effects of intrinsic scatter and the significant spread of distances due to the depth of the cluster.

Visually, most of the points in Figure 4 are within the error bars from the regression line, indicating that the intrinsic scatter is less than the characteristic observational uncertainty. To test this, we compute the generalized reduced χ^2 statistic (e.g., Tremaine et al. 2002; Kelly 2007), defined as

$$\chi^2_{\rm red} = \frac{1}{N-2}\sum_{i=1}^{N}\frac{(y_i-\alpha-\beta x_i)^2}{\sigma_{yi}^2+\beta^2\sigma_{xi}^2}, \quad (5)$$

where α and β are the y-intercept and slope of the linear regression, respectively. For our LSB sample, we find that $\chi^2_{\rm red}=0.70$. Since this is less than 1, the intrinsic scatter is indeed smaller than the observational scatter and is consistent with being zero. Because the intrinsic scatter is necessarily greater than zero, it is likely that some of the observational uncertainties are overestimated, particularly the 0.1 mag uncertainty in the color. From the image simulations, we took this as a characteristic limit of the accuracy of the sky subtraction process, but it is possibly overly conservative for many of the higher surface brightness galaxies. The inferred

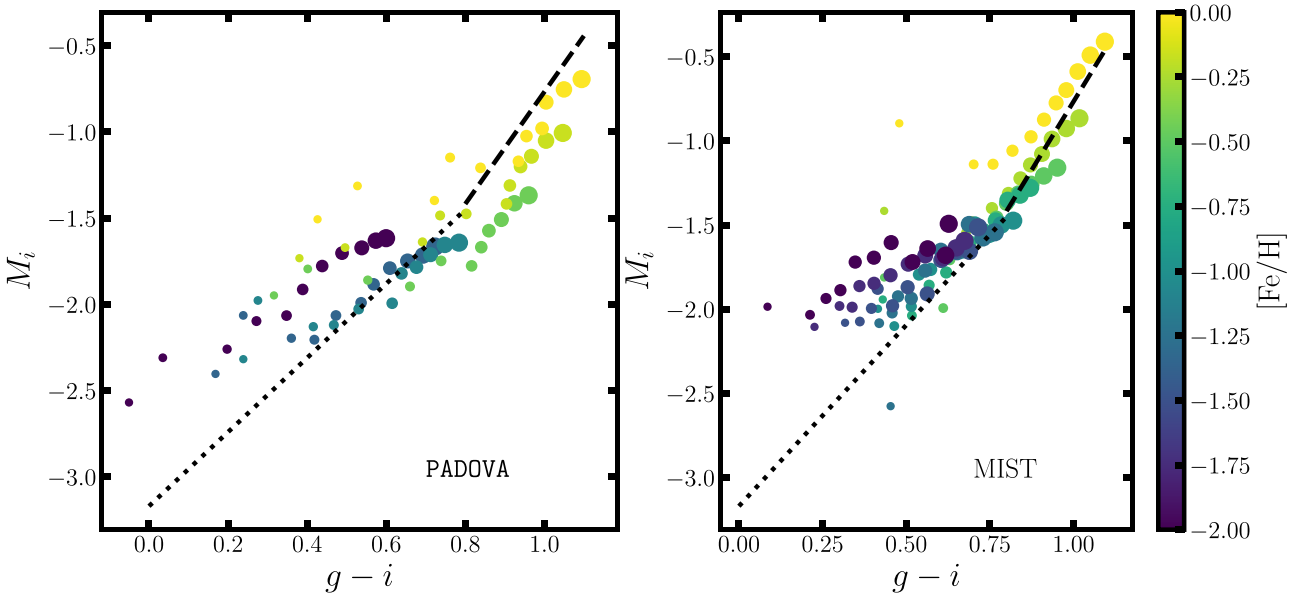

Figure 5. Predicted SBF magnitudes and colors for PARSEC and MIST SSP models in the CFHT filter system. Metallicities in the range $-2 <$ [Fe/H] < 0 and ages in the range 1 Gyr $<$ age $<$ 10 Gyr are shown for both sets of models. Points are colored by metallicity, and the size reflects the age, with biggest points being the oldest. The dashed line is the best-fit calibration of Cantiello et al. (2018). The dotted line shows the regression for our LSB galaxy sample.

intrinsic scatter is clearly very sensitive to the estimated observational uncertainties. Due to the difficulties of estimating the uncertainty introduced by the sky subtraction, we do not attempt to further quantify the intrinsic scatter. Instead, we note that the intrinsic scatter is certainly less than 0.26 mag, which is the residual rms of the regression given in Equation (4). This upper bound is significantly greater than the intrinsic scatter of 0.06 mag estimated for z-band SBF for $g - z > 1.0$ galaxies by Blakeslee et al. (2009). The level of scatter in our sample appears to be roughly similar to that seen for the bluest galaxies in the *HST* IR calibration of Jensen et al. (2015). The rms residual scatter of 0.26 mag (median absolute deviation of 0.21 mag) means that it is possible to measure the distance of these LSB systems to within 15% accuracy, regardless of whether the scatter is intrinsic or not.

4.2. Comparison to Stellar Populations

Since SBF probes the second moment of luminosity of a stellar population, it provides somewhat different information than integrated photometry and can be very useful in studying the stellar populations and population gradients in galaxies (e.g., Cantiello et al. 2007a, 2007b; Mitzkus et al. 2018). However, our main goal in this paper is to provide an empirical SBF calibration for LSB dwarfs to study the satellite systems of nearby massive galaxies, and an in-depth exploration of the stellar populations revealed by SBF is beyond the scope of this study. With that said, it is still interesting to compare our SBF magnitude–color relation with that expected from SPS models.

In Figure 5 we plot the predicted SBF magnitude–color relation from MIST isochrones (Choi et al. 2016) and PARSEC isochrones (Bressan et al. 2012) with the TP-AGB prescription of Marigo et al. (2017) for a range in metallicity and age. Younger and more metal-poor populations are bluer and have brighter SBF magnitudes, as expected. Also shown are the linear regressions for both the LSB galaxy sample and the sample of Cantiello et al. (2018). Qualitatively the models do reproduce some features of the observations. There is an apparent break in the slope in the models around $g - i \sim 0.8$ mag, which is also seen in the observations. However, the observations show a steeper slope in the blue than both sets of models. It is unclear whether this is due to the models or some aspect of the SBF measurement for the very bluest galaxies. Perhaps Sérsic profiles are inadequate, or a significant presence of dust adds extra brightness fluctuations. It is also possible that the bluer galaxies contain intermediate-age AGB stars that are not accurately modeled in the isochrones. We reserve a complete comparison with models for future work.

5. Discussion

In this paper, we have explored the use of SBF in determining the distance to LSB dwarf galaxies, particularly satellite dwarf spheroidals. We have described an SBF measurement procedure that is optimized for small, faint dwarfs by considering the contribution to the SBF signal from faint, undetected background sources. We have shown that SBF measurement is possible for systems with central surface brightness $>$24 mag arcsec^{-2}, size $\sim$10″, and distance out to 10 Mpc with modest ($\sim$hour) exposures on a 4 m telescope. We demonstrated the feasibility of these measurements with realistic image simulations and comparison to existing *HST* measurements.

We provide an empirical SBF calibration that is valid for the blue colors of LSB dwarfs. With 34 galaxies, this is by far the most reliable SBF calibration to date for blue galaxies. Many objects in our galaxy sample are LSB satellite galaxies around nearby massive galaxies, which makes the calibration uniquely adapted for further studies of satellite systems of nearby galaxies since similar stellar populations are expected in these dwarfs. The calibration is given for CFHT g and i bands, which are close to many modern Sloan-like filter sets in use. Our

calibration is also the only calibration to date that is tied completely to TRGB distances. From Figure 3, we see that the zero-point of the calibration agrees quite well with the Cepheid-based SBF zero-point used in previous calibrations (e.g., Cantiello et al. 2018), lending confidence in the modern distance ladder.

The rms scatter of the calibration given in Equation (4) is 0.26 mag. This corresponds to distance measurements with accuracy around 15%. While this is not impressive compared to many modern distance estimators, it is more than adequate for studies of satellite galaxies where there is a strong prior on the distance of the dwarf galaxy. Proximity on the sky and a distance accurate to 15% will be sufficient to determine whether a dwarf is associated with a host in most cases.

Comparing to the predictions of state-of-the-art SSP models, we find modest agreement in both the zero-point of the calibration and the slope. The models predict a shallower slope in the absolute SBF magnitude versus color relation for bluer colors than seen in the data. It is unclear whether this is due to incompleteness in the models or due to something in the SBF measurement process, like Sérsic profiles being inadequate for the very bluest objects.

In conclusion, in this paper we have argued that SBF has been underused in studies of nearby ($D \lesssim 20$ Mpc) LSB dwarf galaxies. We have demonstrated its potential and provided a robust calibration for its use. Distances accurate to $\sim$15% are possible using ground-based data with modest exposure times for even very LSB systems. We note that many of the data sets used to discover LSB dwarfs around nearby massive galaxies are likely of the depth and quality required for SBF distances. In a companion paper (Carlsten et al. 2019), we demonstrate this using the CFHT Legacy Survey data used by Bennet et al. (2017) to discover LSB dwarf satellite candidates around M101. We are able to confirm two galaxies as bona fide companions and 33 out of 43 of the remaining candidates as background galaxies. SBF will be a useful tool in the modern age of deep, wide-field imaging surveys like the Hyper Suprime-Cam Subaru Strategic Program (Aihara et al. 2018) and Large Synoptic Survey Telescope (LSST Science Collaboration et al. 2009), possibly even out to distances of 20 Mpc with very deep ground-based data. While our focus has been on satellite dwarfs, SBF will also be useful in discovering and studying LSB field dwarfs (e.g., Danieli et al. 2018; Greco et al. 2018a, 2018b). The current work opens up the door to many different research goals from galaxy formation and evolution to dark matter studies.

Support for this work was provided by NASA through Hubble Fellowship grant No. 51386.01 awarded to R.L.B. by the Space Telescope Science Institute, which is operated by the Association of Universities for Research in Astronomy, Inc., for NASA, under contract NAS 5-26555. J.P.G. is supported by an NSF Astronomy and Astrophysics Postdoctoral Fellowship under award AST-1801921. J.E.G. and S.G.C. are partially supported by the National Science Foundation grant AST-1713828.

Based on observations obtained with MegaPrime/MegaCam, a joint project of CFHT and CEA/IRFU, at the Canada–France–Hawaii Telescope (CFHT), which is operated by the National Research Council (NRC) of Canada, the Institut National des Science de l'Univers of the Centre National de la Recherche Scientifique (CNRS) of France, and the University of Hawaii. This work is based in part on data products produced at Terapix available at the Canadian Astronomy Data Centre as part of the Canada–France–Hawaii Telescope Legacy Survey, a collaborative project of NRC and CNRS.

Appendix A
SBF Simulations

We used realistic image simulations to further verify our SBF measurements. In the simulations, we use the *i*-band Sérsic fits for the galaxies procured in the SBF measurement to generate artificial galaxies that we then insert into the CCD frames (before sky subtraction). We use isochrones from the MIST project (Choi et al. 2016) to give the artificial galaxies realistic SBF. For a given isochrone, we generate a large sample of stars by sampling a Kroupa IMF (Kroupa 2001). Then, for each pixel in the artificial galaxy, we calculate the expected number of stars in that pixel based on the intensity of the Sérsic profile at that pixel and the average stellar luminosity in the sample of stars from the isochrone.[13] A number is then drawn from a Poisson distribution with mean equal to this expected number of stars. That number of stars is then drawn from the large sample of stars and put into that pixel. This procedure naturally reproduces the SBF magnitude of the population given in Equation (1) and also will exhibit realistic stochasticity in the SBF magnitude owing to partial sampling of the isochrones because of the low stellar mass of many of our galaxies. This procedure also allows us to simultaneously simulate *i*- and *g*-band images of the artificial galaxies. Finally, the galaxies are convolved with a model for the PSF before being inserted into the CCD frames.

We do these simulations for six specific galaxies in our sample: BK5N, NGC 4163, NGC 4258_DF6, M101_DF3, KKH 98, and M94_Dw2. These six were chosen because they have a representative range in surface brightness, size, and exposure time (see Table 1). These six galaxies are shown in Appendix E. BK5N, NGC 4163, and NGC 4258_DF6 were simulated with an [Fe/H] $= -1.5$ and log(age) $= 9.2$ isochrone, and M101_DF3, KKH 98, and M94_Dw2 were simulated with an [Fe/H] $= -0.5$ and log(age) $= 8.3$ isochrone. We emphasize that we do not expect that these stellar populations are actually representative of the galaxies (these are likely much younger than the real galaxies), but these isochrones are chosen because they have absolute SBF magnitudes of $\bar{M}_i = -1.90$ mag and $\bar{M}_i = -2.67$ mag, respectively. These SBF magnitudes are roughly representative of the magnitudes we measure in the actual galaxies (see Section 4). The older isochrone has color $g - i = 0.39$ mag, and the younger isochrone has color $g - i = 0.13$ mag. These are both on the blue side of our galaxy sample, but this does not affect the suitability of the simulations.

For each of these six galaxies, 50 artificial galaxies are generated and inserted somewhere on the CCD chips near the real galaxy (adjacent chips are also used). The chips are processed in the same way as for the real galaxies with the same sky subtraction, resampling, and co-addition process. Each of the artificial galaxies undergoes the same SBF measurement procedure that the real galaxies do. Simulated galaxies that have fitted Sérsic parameters that are more than a factor of two different from the input Sérsic parameters are

[13] The simulated galaxies are assumed to be at the same distance as the real ones that they mimic.

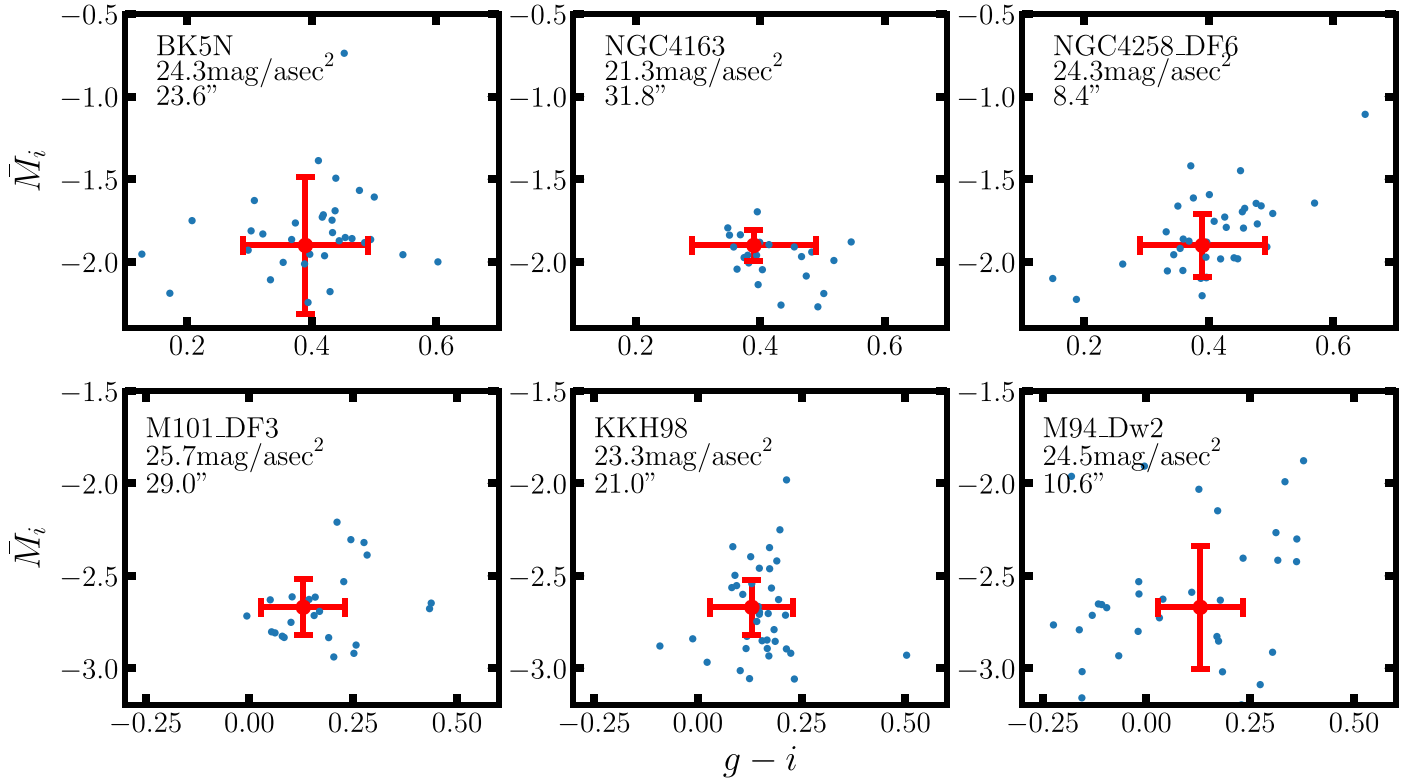

Figure 6. Recovery of the color and SBF magnitude in image simulations for six fiducial galaxies in our sample. The red circle is at the input color and SBF magnitude of the simulated galaxies, and the blue circles show the recovered SBF magnitude and color for each simulated galaxy. The vertical error bars for the red circles are the (1σ) uncertainties calculated for the real galaxy, as described in the text. The horizontal error bars are 0.1 mag, which we take as the contribution to the photometric uncertainty due to the sky subtraction. The galaxy names, central *i*-band surface brightness, and effective radii are listed in the corner of each panel.

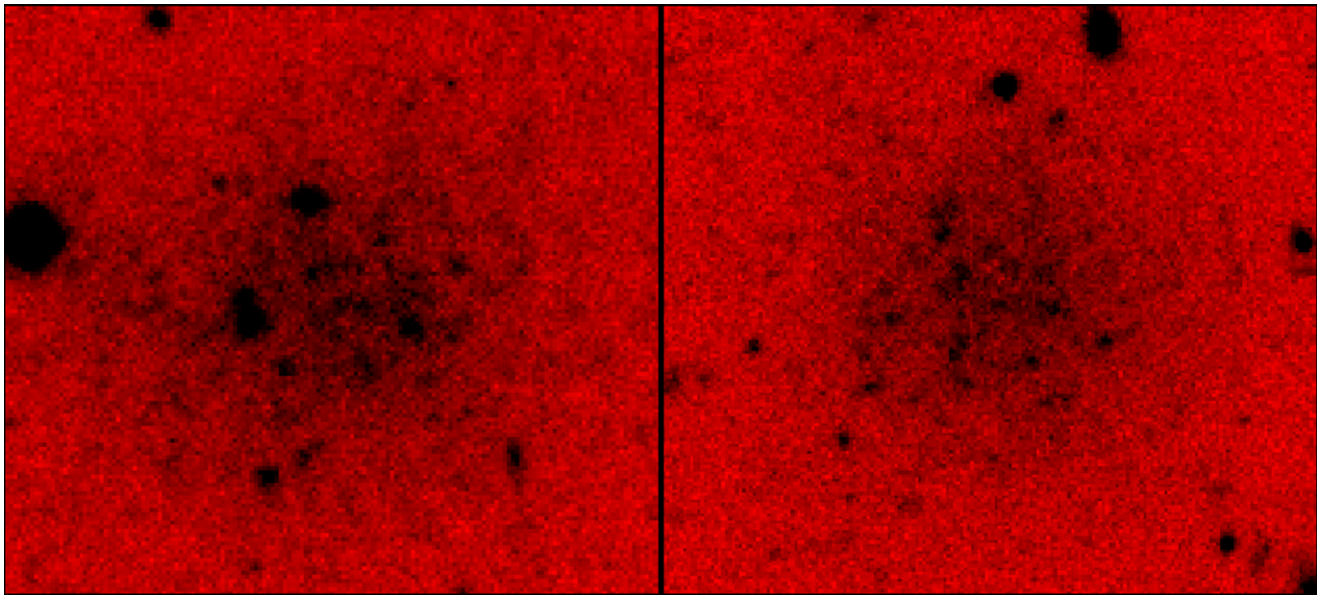

Figure 7. *i*-band images of the real NGC 4258_DF6 galaxy (left) and an artificial galaxy used in the image simulations (right).

removed. These are commonly due to bright foreground stars making the fits unstable. Generally 30–40 artificial galaxies remain for each of the six galaxies. We can then measure the absolute SBF magnitude and color of each of the simulated galaxies and compare with the input values.

Figure 6 shows the results of these simulations for the six fiducial galaxies. The plots show the recovered SBF magnitude and galaxy color of the artificial galaxies compared to the input values. The SBF magnitudes and colors are always concentrated around the input values, verifying our measurement methods. The vertical error bars on the red circles in Figure 6 are the (1σ) uncertainties calculated for each (real) galaxy considering the measurement error and uncertainty in the residual variance, as described above. We see that these error

bars appear to realistically represent the spread in the recovered SBF magnitudes. We take this to indicate that our calculated SBF magnitude uncertainties are realistic and include the dominant sources of error. Regarding the color recovery, we see that the recovered colors are generally precise to $\sim$0.1 mag. This appears to be the limit of our sky subtraction procedure. We include this uncertainty in all of our reported colors and magnitudes. The horizontal error bars in Figure 6 show this 0.1 mag uncertainty. The color recovery for M94_Dw2 appears to be substantially worse than $\pm$0.1 mag. We note that while M94_Dw2 does not have the lowest surface brightness in our galaxy sample, it does have one of the lowest exposure times and is probably the lowest-S/N galaxy in our entire sample. We therefore still take 0.1 mag as a representative uncertainty for the colors of the galaxies owing to the sky subtraction. Figure 7 shows the real NGC 4258_DF6, along with a simulated galaxy.

Appendix B
Details of Data Used

In Table 2 we give further details of the data used in this project, including P.I.s, proposal I.D.s, and the specific filters used.

Table 2
More Information on the Main Galaxy Sample

Name	P.I.	Proposal I.D.	*i* Filter	*g* Filter
FM1	Cuillandre	04BF01, 05AF17	I.MP9701	G.MP9701
UGC 004483	Wilkinson	06BO04	I.MP9701	G.MP9701
KDG 061	Ibata	06AF19	I.MP9701	G.MP9701
BK5N	Cuillandre	06AD97	I.MP9701	G.MP9701
LVJ1228+4358	Higgs	16AD94	I.MP9703	G.MP9702
DDO 125	Higgs	16AD94	I.MP9703	G.MP9702
UGCA 365	Li	13AS03	I.MP9702	G.MP9701
M94_dw2	Li	13AS03	I.MP9702	G.MP9701
DDO 044	Davidge	03BC03	I.MP9701	G.MP9701
NGC 4163	Higgs	16AD94	I.MP9703	G.MP9702
NGC 4190	Higgs	16AD94	I.MP9703	G.MP9701
KDG 090	Higgs	16AD94	I.MP9703	G.MP9701
UGC 08508	Higgs	16AD94	I.MP9703	G.MP9701
DDO 190	Waerbeke	16AC36	I.MP9703	G.MP9701
KKH 98	McConnachie	13AC13, 13BC02	I.MP9702	G.MP9701
Do1	Ibata	03BF10, 05BF48	I.MP9701	G.MP9701
LVJ1218+4655	Harris, Ngeow	10AT01, 11AC08	I.MP9702	G.MP9701
NGC 4258_DF6	Harris, Ngeow	10AT01, 11AC08	I.MP9702	G.MP9701
KDG 101	Harris, Ngeow	10AT01, 11AC08	I.MP9702	G.MP9701
M101_DF1	CFHTLS	05AL02, 06AL99	I.MP9701	G.MP9701
M101_DF2	CFHTLS	05AL02	I.MP9701	G.MP9701
M101_DF3	CFHTLS	08AL05	I.MP9702	G.MP9701
UGC 9405	CFHTLS	07AL02	I.MP9701	G.MP9701
M96_DF9	Duc	09BF07	I.MP9702	G.MP9701
M96_DF1	Cuillandre Duc Harris	09AF05 09BF07 10AD94 11AC08	I.MP9702	G.MP9701
M96_DF8	Duc Harris	09BF07 11AC08	I.MP9702	G.MP9701
M96_DF4	Duc	09AF05 09BF07	I.MP9702	G.MP9701
M96_DF5	Duc Harris	09AF05 09BF07 11AC08	I.MP9702	G.MP9701
M96_DF7	Cuillandre Duc Harris	09BF07 10AD94 11AC08	I.MP9702	G.MP9701
M96_DF10	Duc Harris	09BF07 11AC08	I.MP9702	G.MP9701
M96_DF6	Cuillandre Duc Harris	09AF05 09BF07 10AD94 11AC08	I.MP9702	G.MP9701
M96_DF2	Cuillandre Duc Harris	09AF05 09BF07 10AD94 11AC08	I.MP9702	G.MP9701

Appendix C
Different CFHT Filters

In this appendix we demonstrate that the differences between the various filter generations used in the CFHT data are insignificant. We focus on the difference between the two *g* filters (G.MP9401 and G.MP9402) and the three *i* filters (I.MP9701, I.MP9702, and I.MP9703). We use transforms available online[14] to convert between the different CFHT filters and to external filter systems. From these relations, I.MP9702 differs more from I.MP9701 and I.MP9703 than those two differ from each other. I.MP9701 and I.MP9703 differ at most from each other by $\sim$0.004 mag in the color range of our galaxy sample. I.MP9703 and I.MP9702 differ by $\lesssim$0.035 mag for $r-i\lesssim 0.5$ mag, which will include our sample. G.MP9401 and G.MP9402 differ by $\lesssim$0.06 mag for $g-r\lesssim 0.7$ mag, which is, again, redder than most galaxies in our sample. From these, the effect of the different filters will be fairly insignificant to the color of the measured galaxies. It will be less than the 0.1 mag uncertainty that comes from the sky subtraction process, and we therefore do not try to correct for the different filters in the galaxy photometry.

To explore the effect of the filter on the SBF magnitude, we use the MIST (Choi et al. 2016) isochrones that provide LFs for both I.MP9701 and I.MP9702. In Figure 8, we show the expected difference in SBF magnitude between these two filters as a function of G.MP9401−I.MP9701 color. For the colors of the galaxies in our sample, the difference is $\lesssim$0.07 mag. We note that the difference between I.MP9703 and I.MP9702 will be of a similar size. This difference is generally significantly less than the measurement errors in the SBF measurement, and we do not try to correct for this when making the calibration.

It is possible that the different filters used will contribute to some of the scatter in the calibration, but we found that the scatter is $\lesssim$0.26 mag, which is much greater than the filter effects, which are of the order of 0.05 mag.

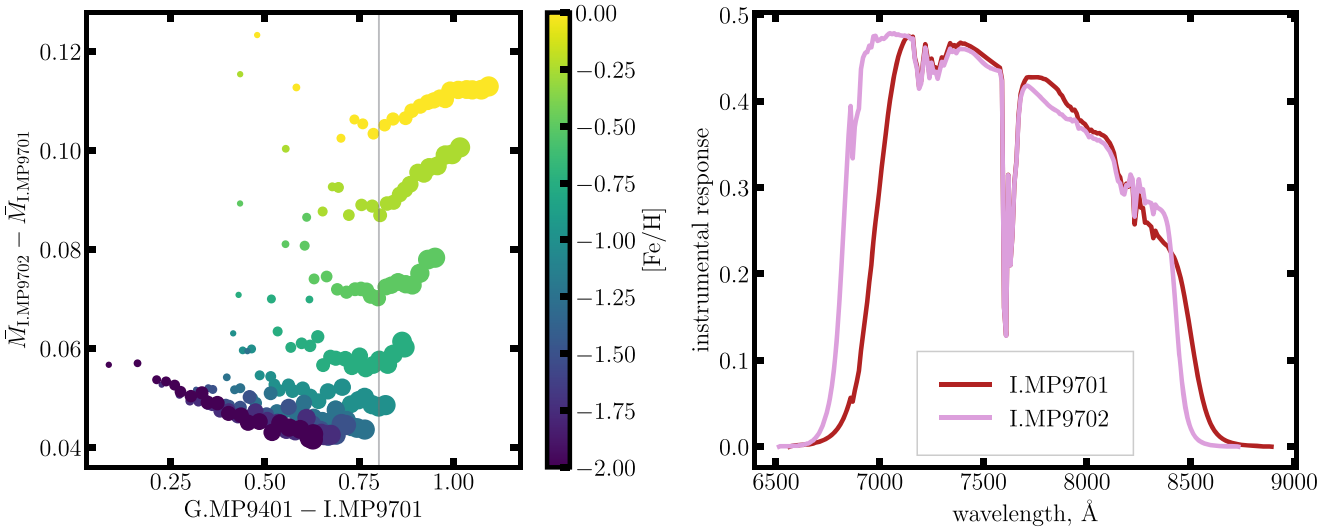

Figure 8. Left: difference in the SBF magnitudes in two of the *i* filters from MIST isochrones vs. color for SSPs in the age range 1 Gyr < age <10 Gyr and metallicity in the range $-2 <$ [Fe/H] < 0. Point size reflects the age, with the biggest points being 10 Gyr populations. The vertical gray line indicates roughly the redward extent of our calibration sample. Right: difference in the instrumental response (including atmospheric absorption) for the two *i* filters.

[14] http://www.cfht.hawaii.edu/Instruments/Imaging/MegaPrime/PDFs/megacam.pdf, http://www.cadc-ccda.hia-iha.nrc-cnrc.gc.ca/en/megapipe/docs/filt.html

Appendix D
Rejected Galaxies

For the sake of completeness, we list the galaxies with TRGB distances in the catalog of Karachentsev et al. (2013) that were not used in the SBF calibration. Table 3 lists these galaxies, along with the primary reason for their exclusion. In the table, "too resolved" refers to the galaxy being too resolved (and often too irregular) for a Sérsic profile to be fit as a model for the smooth galaxy background. Figure 9 shows an example of a galaxy that we put in this category (Holm IX).

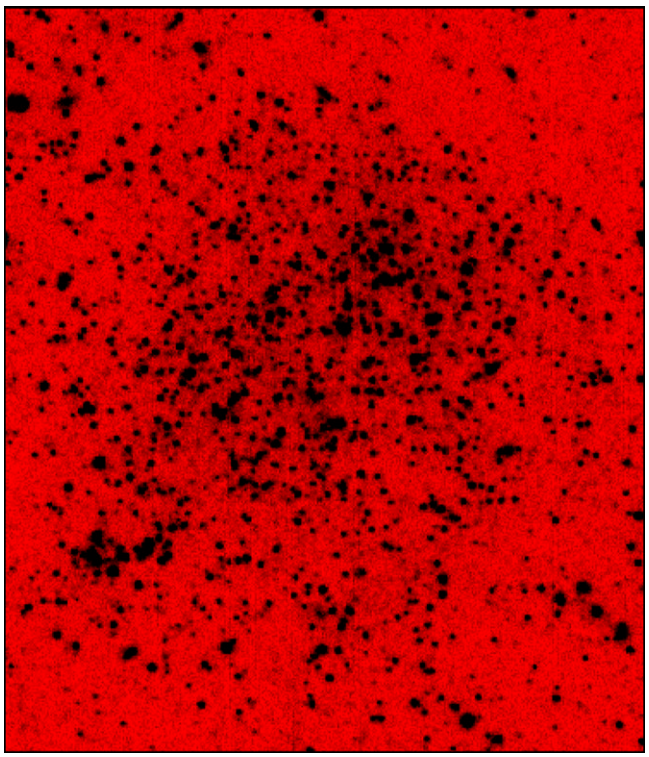

Figure 9. Example of a galaxy (Holm IX) that we consider to be "too resolved" for a smooth galaxy background to be reliably fit.

Table 3
Galaxies Rejected from the Calibration Sample

Name	Reason
And IV	Behind M31's Halo
BK3N	Too resolved
Holm IX	Too resolved
A0952+69	Irregular
d0959+68	Not visible in CFHT data
NGC 3077	Significant dust lanes
Garland	Too resolved
d1005+68	Not visible in CFHT data
MCG+06-27-017	Non-Sérsic
GR34	Non-Sérsic
NGC 4449	Irregular
IC 3583	Irregular
VCC2037	Irregular
dw1335-29	Not visible in CFHT data
KK208	Not visible in CFHT data
Scl-MM-Dw2	Not visible in CFHT data
NGC 404	In halo of extremely bright star
KK35	Too resolved
UGCA 086	Poor-quality CFHT data
NGC 4214	Non-Sérsic
NGC 253	Spiral
NGC 247	Spiral
M81	Spiral
M82	Spiral
NGC 3384	Non-Sérsic
M105	Non-Sérsic
M66	Non-Sérsic
M104	Non-Sérsic
M64	Non-Sérsic
NGC 5102	Non-Sérsic
Cen A	Non-Sérsic
M83	Spiral

Appendix E
Images of Select Galaxies

In Figure 10 we show *i*-band images, masked and normalized images, and power spectra fits for select galaxies. Specifically, Figure 10 shows the six galaxies used in the simulations in the image simulations.

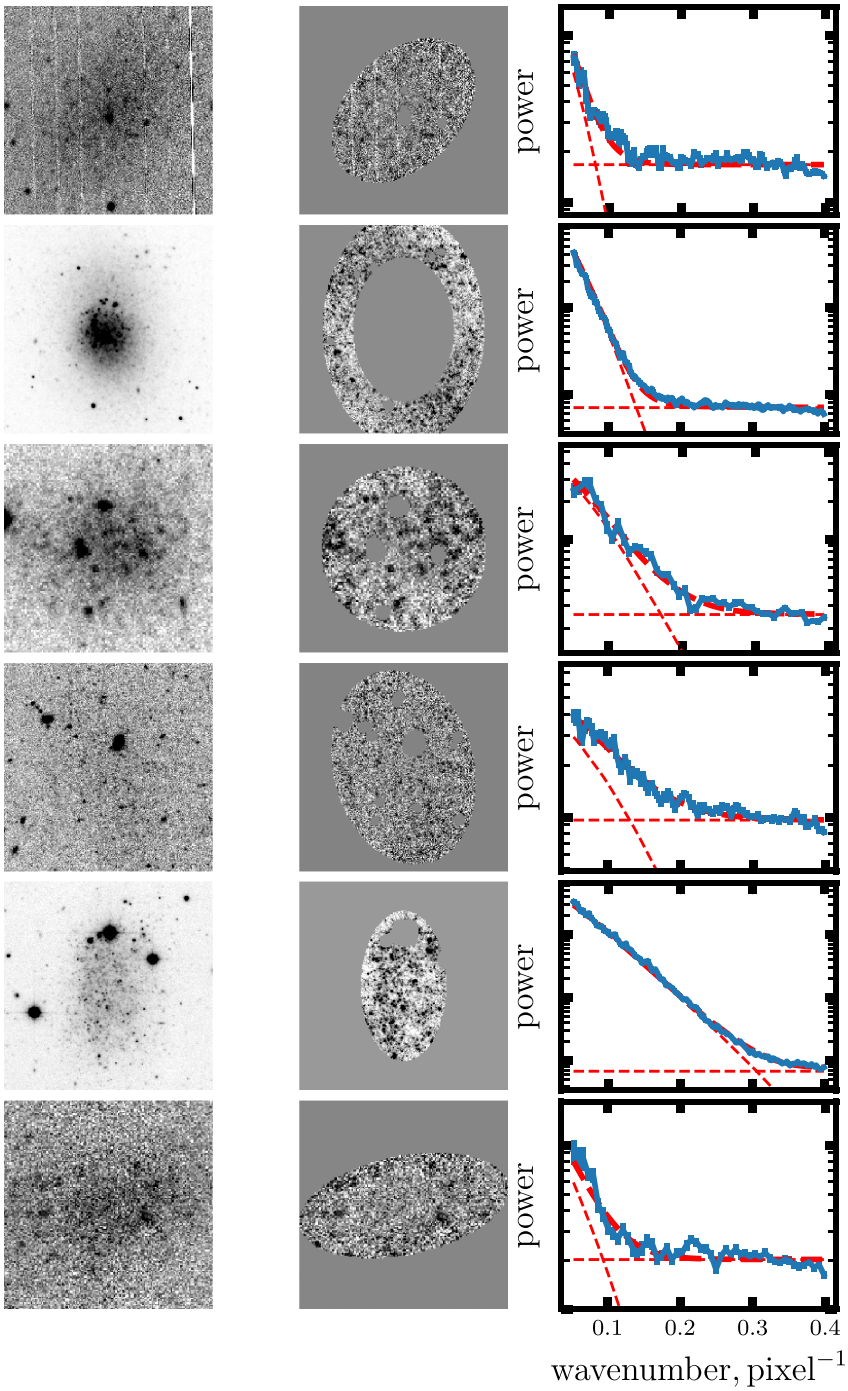

Figure 10. The left panel shows the *i*-band images for the galaxy, middle panel shows the masked and normalized images, and the right panel shows the fluctuation power spectrum and fit. The galaxies are, in order from top to bottom, BK5N, NGC 4163, NGC 4256-DF6, M101-DF3, KKH 98, and M94-Dw2.

ORCID iDs

Scott G. Carlsten https://orcid.org/0000-0002-5382-2898
Rachael L. Beaton https://orcid.org/0000-0002-1691-8217
Johnny P. Greco https://orcid.org/0000-0003-4970-2874

References

Abolfathi, B., Aguado, D. S., Aguilar, G., et al. 2018, ApJS, 235, 42
Abraham, R. G., & van Dokkum, P. G. 2014, PASP, 126, 55
Ahn, C. P., Alexandroff, R., Allende Prieto, C., et al. 2012, ApJS, 203, 21
Aihara, H., Arimoto, N., Armstrong, R., et al. 2018, PASJ, 70, S4
Ajhar, E. A., & Tonry, J. L. 1994, ApJ, 429, 557
Barbary, K. 2016, JOSS, 1, 58
Beaton, R. L., Bono, G., Braga, V. F., et al. 2018, SSRv, 214, 113
Bennet, P., Sand, D. J., Crnojević, D., et al. 2017, ApJ, 850, 109
Bertin, E. 2006, in ASP Conf. Ser. 351, Astronomical Data Analysis Software and Systems XV, ed. C. Gabriel et al. (San Francisco, CA: ASP), 112
Bertin, E. 2010, SWarp: Resampling and Co-adding FITS Images Together, Astrophysics Source Code Library, ascl:1010.068
Bertin, E., & Arnouts, S. 1996, A&AS, 117, 393
Blakeslee, J. P., & Cantiello, M. 2018, RNAAS, 2, 146
Blakeslee, J. P., Cantiello, M., Mei, S., et al. 2010, ApJ, 724, 657
Blakeslee, J. P., Jordán, A., Mei, S., et al. 2009, ApJ, 694, 556
Boulade, O., Charlot, X., Abbon, P., et al. 2003, Proc. SPIE, 4841, 72
Bressan, A., Marigo, P., Girardi, L., et al. 2012, MNRAS, 427, 127
Bullock, J. S., & Boylan-Kolchin, M. 2017, ARA&A, 55, 343

Cantiello, M., Blakeslee, J., Raimondo, G., Brocato, E., & Capaccioli, M. 2007a, ApJ, 668, 130
Cantiello, M., Blakeslee, J. P., Ferrarese, L., et al. 2018, ApJ, 856, 126
Cantiello, M., Blakeslee, J. P., Raimondo, G., et al. 2005, ApJ, 634, 239
Cantiello, M., Raimondo, G., Blakeslee, J. P., Brocato, E., & Capaccioli, M. 2007b, ApJ, 662, 940
Cantiello, M., Raimondo, G., Brocato, E., & Capaccioli, M. 2003, AJ, 125, 2783
Carlin, J. L., Sand, D. J., Price, P., et al. 2016, ApJL, 828, L5
Carlsten, S., Beaton, R., Greco, J., & Greene, J. 2019, ApJ, 878, 16
Carlsten, S. G., Strauss, M. A., Lupton, R. H., Meyers, J. E., & Miyazaki, S. 2018, MNRAS, 479, 1491
Chambers, K. C., Magnier, E. A., Metcalfe, N., et al. 2016, arXiv:1612.05560
Choi, J., Dotter, A., Conroy, C., et al. 2016, ApJ, 823, 102
Cohen, Y., van Dokkum, P., Danieli, S., et al. 2018, ApJ, 868, 96
Crnojević, D., Sand, D. J., Caldwell, N., et al. 2014, ApJL, 795, L35
Danieli, S., van Dokkum, P., & Conroy, C. 2018, ApJ, 856, 69
Danieli, S., van Dokkum, P., Merritt, A., et al. 2017, ApJ, 837, 136
Duc, P.-A., Cuillandre, J.-C., Karabal, E., et al. 2015, MNRAS, 446, 120
Dunn, L. P., & Jerjen, H. 2006, AJ, 132, 1384
Erwin, P. 2015, ApJ, 799, 226
Ferrarese, L., Côté, P., Cuillandre, J.-C., et al. 2012, ApJS, 200, 4
Forbes, D. A., Read, J. I., Gieles, M., & Collins, M. L. M. 2018, MNRAS, 481, 5592
Foreman-Mackey, D. 2016, JOSS, 1, 24
Geha, M., Wechsler, R. H., Mao, Y.-Y., et al. 2017, ApJ, 847, 4
Greco, J. P., Goulding, A. D., Greene, J. E., et al. 2018a, ApJ, 866, 112
Greco, J. P., Greene, J. E., Strauss, M. A., et al. 2018b, ApJ, 857, 104
Gwyn, S. D. J. 2008, PASP, 120, 212
Hogg, D. W., Bovy, J., & Lang, D. 2010, arXiv:1008.4686
Ibata, R. A., Lewis, G. F., Conn, A. R., et al. 2013, Natur, 493, 62
Jang, I. S., Hatt, D., Beaton, R. L., et al. 2018, ApJ, 852, 60
Jedrzejewski, R. I. 1987, MNRAS, 226, 747
Jensen, J. B., Blakeslee, J. P., Gibson, Z., et al. 2015, ApJ, 808, 91
Jensen, J. B., Tonry, J. L., Barris, B. J., et al. 2003, ApJ, 583, 712
Jensen, J. B., Tonry, J. L., & Luppino, G. A. 1998, ApJ, 505, 111
Jerjen, H. 2003, A&A, 398, 63
Jerjen, H., Binggeli, B., & Barazza, F. D. 2004, AJ, 127, 771
Jerjen, H., Freeman, K. C., & Binggeli, B. 1998, AJ, 116, 2873
Jerjen, H., Freeman, K. C., & Binggeli, B. 2000, AJ, 119, 166
Jerjen, H., Rekola, R., Takalo, L., Coleman, M., & Valtonen, M. 2001, A&A, 380, 90
Karachentsev, I. D., Makarov, D. I., & Kaisina, E. I. 2013, AJ, 145, 101
Kelly, B. C. 2007, ApJ, 665, 1489
Kim, E., Kim, M., Hwang, N., et al. 2011, MNRAS, 412, 1881
Kondapally, R., Russell, G. A., Conselice, C. J., & Penny, S. J. 2018, MNRAS, 481, 1759
Kroupa, P. 2001, MNRAS, 322, 231
Law, D. R., & Majewski, S. R. 2010, ApJ, 718, 1128
LSST Science Collaboration, Abell, P. A., Allison, J., et al. 2009, arXiv:0912.0201
Macciò, A. V., Kang, X., Fontanot, F., et al. 2010, MNRAS, 402, 1995
Magnier, E. A., & Cuillandre, J.-C. 2004, PASP, 116, 449
Marigo, P., Girardi, L., Bressan, A., et al. 2017, ApJ, 835, 77
Martinez-Delgado, D., Grebel, E. K., Javanmardi, B., et al. 2018, A&A, 620, 126
Mei, S., Blakeslee, J. P., Tonry, J. L., et al. 2005a, ApJ, 625, 121
Mei, S., Blakeslee, J. P., Tonry, J. L., et al. 2005b, ApJS, 156, 113
Merritt, A., van Dokkum, P., Danieli, S., et al. 2016, ApJ, 833, 168
Mieske, S., Hilker, M., & Infante, L. 2003, A&A, 403, 43
Mieske, S., Hilker, M., & Infante, L. 2006, A&A, 458, 1013
Mieske, S., Hilker, M., Infante, L., & Mendes de Oliveira, C. 2007, A&A, 463, 503
Mitzkus, M., Walcher, C. J., Roth, M. M., et al. 2018, MNRAS, 480, 629
Monet, D. G., Levine, S. E., Canzian, B., et al. 2003, AJ, 125, 984
Müller, O., Jerjen, H., & Binggeli, B. 2017a, A&A, 597, A7
Müller, O., Jerjen, H., & Binggeli, B. 2018a, A&A, 615, A105
Müller, O., Pawlowski, M. S., Jerjen, H., & Lelli, F. 2018b, Sci, 359, 534
Müller, O., Rejkuba, M., & Jerjen, H. 2018c, A&A, 615, A96
Müller, O., Scalera, R., Binggeli, B., & Jerjen, H. 2017b, A&A, 602, A119
Park, H. S., Moon, D.-S., Zaritsky, D., et al. 2017, ApJ, 848, 19
Pawlowski, M. S. 2018, MPLA, 33, 1830004
Pawlowski, M. S., Pflamm-Altenburg, J., & Kroupa, P. 2012, MNRAS, 423, 1109
Rekola, R., Jerjen, H., & Flynn, C. 2005, A&A, 437, 823
Sand, D. J., Crnojević, D., Strader, J., et al. 2014, ApJL, 793, L7
Schlafly, E. F., & Finkbeiner, D. P. 2011, ApJ, 737, 103
Schlegel, D. J., Finkbeiner, D. P., & Davis, M. 1998, ApJ, 500, 525
Smercina, A., Bell, E. F., Price, P. A., et al. 2018, ApJ, 863, 152
Smercina, A., Bell, E. F., Slater, C. T., et al. 2017, ApJL, 843, L6
Speller, R., & Taylor, J. E. 2014, ApJ, 788, 188
Spencer, M., Loebman, S., & Yoachim, P. 2014, ApJ, 788, 146
Tanaka, M., Chiba, M., Hayashi, K., et al. 2018, ApJ, 865, 125
Tonry, J., & Schneider, D. P. 1988, AJ, 96, 807
Tonry, J. L., Dressler, A., Blakeslee, J. P., et al. 2001, ApJ, 546, 681
Tremaine, S., Gebhardt, K., Bender, R., et al. 2002, ApJ, 574, 740
Trujillo, I., Beasley, M. A., Borlaff, A., et al. 2019, MNRAS, 486, 1192
van Dokkum, P., Danieli, S., Cohen, Y., et al. 2018b, Natur, 555, 629
van Dokkum, P., Danieli, S., Cohen, Y., Romanowsky, A. J., & Conroy, C. 2018a, ApJL, 864, L18
Wetzel, A. R., Hopkins, P. F., Kim, J.-h., et al. 2016, ApJL, 827, L23
Xi, C., Taylor, J. E., Massey, R. J., et al. 2018, MNRAS, 478, 5336